

## Article

# Structural and Electrochemical Properties of *Musa acuminata* Fiber Derived Hard Carbon as Anodes of Sodium-Ion Batteries

Meenatchi Thenappan<sup>1</sup>, Kouthaman Mathiyalagan<sup>1</sup>, Mozaffar Abdollahifar<sup>2,3,\*</sup> , Subadevi Rengapillai<sup>1,\*</sup> and Sivakumar Marimuthu<sup>1,\*</sup> 

<sup>1</sup> #120, Energy Materials Lab, Department of Physics, Science Block, Alagappa University, Karaikudi 630003, Tamil Nadu, India

<sup>2</sup> Institute for Particle Technology, Technische Universität Braunschweig, Volkmaroder Str. 5, 38104 Braunschweig, Germany

<sup>3</sup> Battery LabFactory Braunschweig (BLB), Technische Universität Braunschweig, Langer Kamp 19, 38106 Braunschweig, Germany

\* Correspondence: m.abdollahifar@tu-braunschweig.de (M.A.); susimsk@yahoo.co.in or subadevir@alagappauniversity.ac.in (S.R.); susiva73@yahoo.co.in or sivakumarm@alagappauniversity.ac.in (S.M.); Tel.: +49-531-391-94664 (M.A.); +91-4565223306 (S.R.); +91-4565223304 (S.M.)

**Abstract:** Hard carbon (HC) was successfully synthesized using a bio-waste precursor from *Musa acuminata* fiber (MaF) as an eco-friendly option through the pyrolysis process at 500 °C. Further, it was activated using the chemical activating agents, NaOH and ZnCl<sub>2</sub>, at 900 °C, named Na–MaFDHC and Zn–MaFDHC. The MaFDHCs are employed as anode materials for emerging sodium-ion batteries (NIBs). The nitrogen (N<sub>2</sub>) adsorption and desorption studies and HRTEM images resulted that the MaFDHCs have a mesoporous nature. The surface area and pore diameter of the carbon materials are increased significantly after the treatment with activating agents, which are important factors for anodes of NIBs. The electrochemical performance of the MaFDHCs depends on the activation agent. Zn–MaFDHC with a higher surface area showed better results, yielding a charge capacity of about 114 mAh g<sup>-1</sup> at a 1C rate.

**Keywords:** hard carbon; pyrolysis; activating agents; anode; sodium-ion batteries



**Citation:** Thenappan, M.; Mathiyalagan, K.; Abdollahifar, M.; Rengapillai, S.; Marimuthu, S. Structural and Electrochemical Properties of *Musa acuminata* Fiber Derived Hard Carbon as Anodes of Sodium-Ion Batteries. *Energies* **2023**, *16*, 979. <https://doi.org/10.3390/en16020979>

Academic Editors: Haifeng Dai, Michael Knapp, Jiangong Zhu and Mario Aparicio

Received: 12 October 2022  
Revised: 28 December 2022  
Accepted: 13 January 2023  
Published: 15 January 2023



**Copyright:** © 2023 by the authors. Licensee MDPI, Basel, Switzerland. This article is an open access article distributed under the terms and conditions of the Creative Commons Attribution (CC BY) license (<https://creativecommons.org/licenses/by/4.0/>).

## 1. Introduction

In this rapid technologically upgrading world, energy demand is rising exponentially as fossil fuel prices are escalating swiftly [1]. Hence, a crucial factor is fulfilling the need for energy demand for the vast world's population. The most important global concern is energy storage, due to climate change and the minimum availability of fossil fuels, that dictates the selection of an alternative energy storage technology. Among the variety of alternate energy resources, battery technology has spread its fame worldwide due to its enticing properties such as high energy and power density. Secondary batteries have engendered much attention in portable electronic devices such as electric vehicles and renewable power stations. Lithium-ion batteries (LIBs) are esteemed as the most promising type in battery technology [2,3]. As the utility of the battery is becoming higher day by day, the lithium source is being consumed enormously, leading to higher prices in the market [4]. To mitigate these hurdles, sodium-ion batteries (NIBs) for stationary storage systems are considered a suitable substitute for LIBs. NIBs are fully drained without damaging the active materials, i.e., completely discharged to zero volts [5]. Hence, they can be shipped safely and stored. Whereas, in the case of Li<sup>+</sup>, it will retain partial charge in order to eliminate short-circuiting during storage, NIBs also have excellent EC features in terms of reversibility, charge–discharge and specific capacity. Several of the literature reports and articles have discussed the accessibility of constructing nanostructured materials or

addressing the problem of fast capacity fading and structure degradation [6,7]. Fundamentally, graphite is considered to be the anode for LIBs. When this graphite is used in NIBs, it has a low capacity as the Na-ions cannot be intercalated into the graphite, owing to its large ionic radius (1.02 Å) [8]. Incredible efforts are made to employ a suitable substitute anode material for SIBs. Metal oxides, alloy-type materials [9], phosphorous and carbonaceous materials [10] have also been investigated for their performance. One capable candidate for commercializing NIBs is hard carbon (HC), otherwise called non-graphitizable carbon. Its structure is short, highly curved, and defective graphenic nanosheets are oriented randomly and loosely stacked with vast Van Der Waals distances. Owing to the large interlayer distance, it can act as a host for Na-ions so that these ions undergo easy intercalation into their respective storage sites [11]. The pyrolysis of biomass can easily attain HC because the O/C ratio in the carbon precursors is large, leading to the formation of a disordered and amorphous structure of HC. As a result of the pyrolysis of the materials, the breaking of hydrogen bonds occurs and leads to decomposing of the organic materials such as lignin, cellulose and hemicellulose. This may result in a more porous nature of the synthesized materials. These pores or voids can accommodate more Na-ions during the intercalation through pores. The defects and porosity were considered to be necessary to further improve the capacity and EC performance of HC.

Several biomass precursors, such as lignocellulosic materials [12] (rice husk [13], date palm seeds [14], coconut shell [15], wood [16], fruit bunch [17], bamboo [18], corncob residue [19], waste tea leaves [20], olive cake [21], and oil palm trunk [22], orange peel [23]), have been conventionally employed so far to improve the porosity of carbon. The commonly used chemical activating agents for enhancing the porosity of HC are NaOH, KOH, H<sub>3</sub>PO<sub>4</sub>, and ZnCl<sub>2</sub> [24,25]. Among them, NaOH and ZnCl<sub>2</sub> are the most appetizing chemical activators. Basically, the chemical activating agents have been used to activate the bio precursors. When compared to KOH, NaOH is cost effective material. They have similar chemical properties of KOH. H<sub>3</sub>PO<sub>4</sub> is an acidic reagent. It is more corrosive, but harmful. Hence, the safer and cost effective NaOH and ZnCl<sub>2</sub> are preferable. The chemical activation can improve the structural stability and morphology of the material. They act as a dehydrating agent and can affect the pyrolytic decomposition. As a result, it produces tar which is responsible for the high carbon yield. The main advantage of these reagents is that they can produce high yield carbon, high porosity, surface area, and precise pore size distribution [26]. Natural fibrous materials are low-cost and compostable. There are a variety of fibrous materials available in developing countries. They are sisal, jute, coir, *Musa acuminata* (*Ma*), etc. In recent years, these materials have been utilized in a typical manner for the production of mats, yarn, hangings, handbags, and purses. Among them, *Ma* is extensively obtained and is appraised as one of the world's most beneficial plants. This plant belongs to the Musaceae family. It is considered to be more enticing, as most of the parts can be served for multifarious purposes such as various edible as well as non-edible applications such as flavoring and coolant thickener, fibers, livestock feed, bioactive organic fertilizers, and multiple sources [27]. Regarding several articles, it can be assessed that a *Ma* farm could yield approximately 220 tons of waste [28]. They are burnt and also disposed of in rivers and lakes. If this waste is not managed properly, they may harm and pollute society. It releases CO<sub>2</sub> along with noxious gas and leads to greenhouse gas. In this sense, these *Ma* wastes can be used more rationally to fabricate HC for batteries, supercapacitors, and textile industries. Venkateshwara et al. [29] reviewed the various fibrous materials and delineated the values of width and elongation percentage of the materials. They reported the density, tensile strength, tensile modulus, and elongation of fibrous materials. Due to these properties, the materials have been used in various fields such as automotive machinery, construction, etc. Table S1, and Figures S1 and S2, describe the physical properties of the fibers. In general, the elongation percentage, i.e., the natural expansion of the plant fiber, is a significant factor that affects the ion transfer process. Comparing the various fibrous materials reported in Venkateshwara analysis, *Ma*

fiber (MaF) shows high width and low elongation percentage. In accordance with this, MaF materials have stable structural stability properties as opposed to other materials.

In this work, we probed the idea that HC can be electrochemically active for NIBs. The chief precedence of the present carbonaceous material is its bio precursor, i.e., banana fibers. Particularly, the utilization of the carbon electrode material acquired by the pyrolysis process of banana fibers as a natural cellulose-based precursor has not been addressed in the literature for NIB applications. This leads to investigating the prospects of using carbon electrode materials derived from the banana fiber precursor. NIBs require high pore volume and a highly disordered structure for the ion transfer process. Here, the activating agents used are NaOH and ZnCl<sub>2</sub>, which enlarges the porosity of HC for the ion transfer process. The following are the unique properties of MaF.

- (i) MaF is cost-effective, environmentally friendly, and available worldwide.
- (ii) MaF has stable structural properties (i.e., low elongation percentage) and high width responsible for the ion transfer process.
- (iii) MaF has a distinctive porous structure. It leads to better intercalation and deintercalation of Na ions.
- (iv) Basically, MaF has 50.9% of carbon content in it. This induces the conductivity of the material.

The main theme behind the synthesis is utilizing the MaF, an abundant waste product, to make electrodes for renewable and storage purposes. All the physical and electrochemical characterizations were performed, and the analyzed results, were reported in detail.

## 2. Experimental Procedure

### 2.1. Preparation of MaF Derived Hard Carbon (MaFDHC)

The MaF was chopped into small pieces and dried at 220 °C overnight. Then, the samples were pyrolyzed under argon flow at 500 °C for 2 h with a heat rate of 5 °C min<sup>-1</sup>. In this work, NaOH and ZnCl<sub>2</sub> are used as the chemical activating agents. The MaF precursor was immersed into the activating agents (7%) at room temperature and then dehumidified at 110 °C for 24 h. The obtained MaF powder was then pyrolyzed at 900 °C for 2 h at 5 °C min<sup>-1</sup> heat rate under an argon atmosphere. The pyrolyzed powders were then milled and cleaned with 2 M HCl and distilled water several times, and dried at 110 °C for 24 h. MaFDHC using NaOH and ZnCl<sub>2</sub> are named Na-MaFDHC and Zn-MaFDHC, respectively. The schematic representation for the synthesis of MaFDHC is shown in Figure 1.



**Figure 1.** Synthesis processes of MaFDHC powders.

### 2.2. Structural Characterizations

The degradation and weight loss of the sample were confirmed by thermogravimetry analysis (TGA) and differential thermal analysis (DTA) (SIINT 6300 TG DTA). The FT-IR characterizations were analyzed (PerkinElmer) in the range of 4000–400 cm<sup>-1</sup>. The nature

of the material was analyzed by powder X-ray diffraction (XRD) analysis (PAN analytical, X'pert pro model) with Cu K $\alpha$ . The Raman spectroscopy was carried out using STR RAMAN, SEKI Corporation, Japan, to categorize and confirm the occurrence of carbon phases. The structural morphology of the as-prepared sample was determined by scanning electron microscopy (SEM) using Quanta FEG 250. High-Resolution Transmission electron microscopy (HRTEM) was performed using JEOL Hi-Resolution Transmission Electron Microscope, Tokyo, Japan. N<sub>2</sub> adsorption/desorption isotherms were carried out by Nova station A at 77 K.

### 2.3. Cell Fabrication and Electrochemical Measurements

The electrochemical performance of the synthesized materials was analyzed using a coin-cell (CR-2032 type) that was assembled under an argon (Ar) filled glove box. The negative electrodes coated onto an aluminum foil were comprised of the mixture of active material, carbon black Super-P (alfa aesar), and poly (vinylidene fluoride) (PVdF) (alfa aesar) with a mass ratio of 75:15:10 in N-Methyl-2-Pyrrolidone, NMP, (alfa aesar) as solvent. The mass loading for electrodes was about 3.4 mg cm<sup>-2</sup>. Circular electrodes with a diameter of 10 mm were punched and dried under vacuum at 60 °C. The coin cells were assembled in an Ar-filled glove box using a glass fiber and 200  $\mu$ L of electrolyte (1.0 M NaClO<sub>4</sub> dissolved in diethylene carbonate (DEC)/ethylene carbonate (EC), 1:1 ratio *v:v*). The electrochemical measurements were carried out using a Biologic Seyssinet-Pariset (BCS-815, Seyssinet-Pariset, France) battery tester at ambient temperature. The cells were evaluated within a voltage window of 0.2–3.0 V vs. Na/Na<sup>+</sup> and 100 cycles were performed at 1 C rate. Electrochemical impedance spectra (EIS) were recorded with an AC amplitude of 10 mV using Biologic (BCS-815, France) battery tester, with a frequency from 10 KHz to 1 Hz. EIS measurements were performed after the electrodes reached the end of discharge and relaxed for one day to let the potential stabilize.

## 3. Results and Discussion

The TG-DTA graph for the raw MaF is shown in Figure 2a. The Thermogravimetric (TG) analysis is used to analyze the thermal degradation/stability of the MaF. The morphology of MaF is mainly composed of biopolymers in the plant cell walls. It comprises sugar, proteins, hemicellulose, pectin, lignin, and some crystalline cellulose. Here, lignin and hemicellulose are both cross-linked and non-crystalline in nature. It results in the formation of non-graphitic carbon at pyrolysis temperature. Particularly, lignin plays a remarkable role in changing biomass into carbonaceous material over pyrolysis. Pectin, which is analogous in structure to lignin, consists of sugar monomers. Normally, the organic molecules emit gases such as CO and CH<sub>4</sub> during pyrolysis. The remaining cross-linked carbon undergoes several aromatic orderings. Whenever the organic molecule precursors are rich in smaller biopolymer molecules such as free sugar, a viscous liquid may be formed, allowing the partial alignment of carbon atoms. The thermal degradation of the sample initially starts from 30 °C. The initial weight loss (~10%) occurs between 30 and 144 °C. It is observed that, from 30 °C, the release of weakly bound water molecules takes place, i.e., humidity loss. During 200–260 °C, the second main weight loss of ~25% occurs. At this point, an exothermic peak arises due to the hemicellulose degradation. It consists of mannose, glucose, galactose, arabinose and xylase [30]. Cellulose degradation starts at approximately 296 °C; subsequently the degradation of hemicellulose takes place [24]. It forms a long chain, bonded with each other by hydrogen bonds. Finally, lignin degradation takes place gradually at the temperature up to 550 °C [31]. In addition, it can be noticed that DTA has the same decomposition profile joined with intense exothermic peaks. The DTA peaks are related to the thermal decomposition of organic materials [32]. Thus, the TG-DTA analysis shows that the banana fiber is a Nobel precursor for NIB, which prevents the crystallization of graphite by balancing the lignin and pectin, which enables the fractional ordering of the graphene layers [30]. However, the subsequent graphene sheets are also

highly disordered, i.e., non-graphitizable. This non-graphitic ordering allows substantial Na intercalation/deintercalation during cycling.

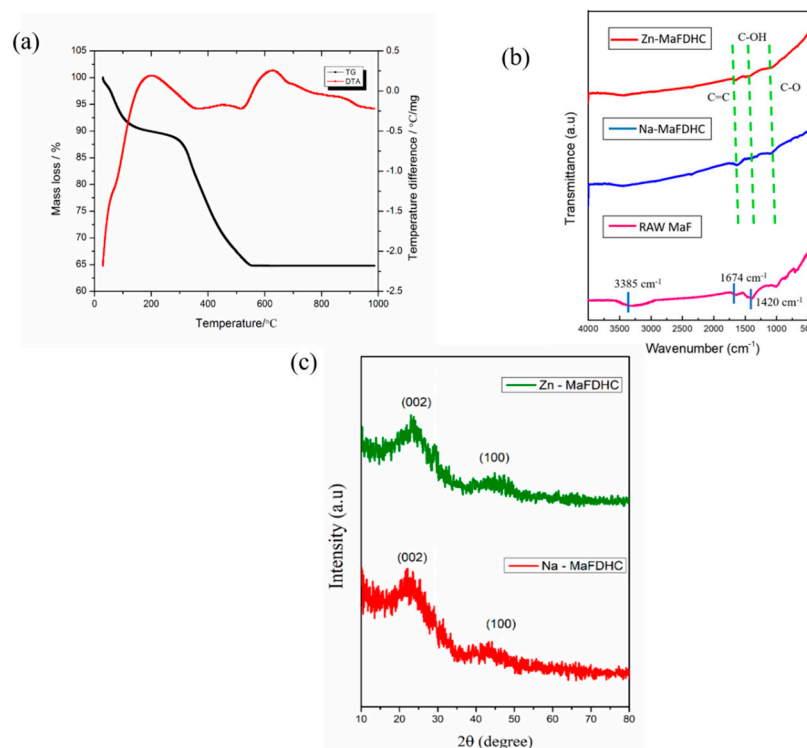


**Figure 2.** (a) TG/DTA of raw MaF. (b) FT-IR spectrum of Na-MaFDHC and Zn-MaFDHC, (c) XRD pattern of Na-MaFDHC and Zn-MaFDHC powders.

The FT-IR was used to analyze the functional groups in the untreated MaF and treated MaFDHC. Figure 2b shows the FT-IR spectra of the raw MaF and treated MaFDHC. The FT-IR spectra also confirms that the raw MaF contains hemicellulose, cellulose and lignin content, i.e., biopolymers, which is in agreement with TGA analysis. In the untreated and raw MaF sample, the band at  $3385\text{ cm}^{-1}$  corresponds to lignin and the bands at  $1675$  and  $1420\text{ cm}^{-1}$  are attributed to the presence of hemicellulose and cellulose [33,34]. The peaks at  $1000\text{--}1200\text{ cm}^{-1}$  insists on the presence of C-O-C asymmetric stretching vibrations. It can be seen that the treated MaFDHC shows characteristic functional groups. The bands at  $1083$ ,  $1473$  and  $1646\text{ cm}^{-1}$  gave the absorption spectra of C-O, C-OH and C=C, respectively. By comparing the untreated MaF and treated MaFDHC, the lignin and hemicellulose components nearly vanished after the carbonization process. This is due to breaking hydrogen bonds in O-H groups of cellulose and hemicellulose components. It confirms that the organic bonds (cellulose, hemicellulose and lignin) are entirely decomposed to form hard carbon materials.

The XRD patterns of MaFDHC are shown in Figure 2c. The Xrd patterns of the raw MaF are shown in Figure S3. Two peaks at  $2\theta = 17^\circ$  and  $24^\circ$ , corresponding to (110) and (002). This peak at (110) represents the cellulose crystallographic plane [34]. The XRD patterns indicate that Na-MaFDHC and Zn-MaFDHC have a disordered structure consisting of one strong broad peak at  $2\theta = 23^\circ$  and one weak broad peak at  $43^\circ$ , corresponding to (002) and (100) diffraction planes [35,36]. For the as-prepared samples, the disordered structure was confirmed by the wide shapes of the perceived peaks. The d-spacing ( $d_{(002)}$ ,  $d_{(100)}$ ) has been used to ascertain the structure. When compared to graphite ( $0.3354\text{ nm}$ ), the d-spacing of hard carbon ( $0.36\text{ nm}$ ) is increased [23,37,38]. This interlayer spacing plays a vital role in the interaction and deintercalation of sodium ions. Due to the higher ionic radius of sodium, it requires a more suitable anode material than graphite. The disorderly structure

and the higher interlayer spacing make the MaFDHC an alternative anode material for sodium ion batteries.

Figure 3 displays the Raman spectrum of Na–MaFDHC and Zn–MaFDHC samples and Figure S4 shows the Raman spectrum of raw MaF. In the Raman spectrum for carbonaceous material, the D band is commensurate to the disordered carbon and the G band is for graphitic layers related to the tangential vibrations of carbon atoms. The intensity ratio of these two peaks reveals the degree of graphitic ordering in the carbons. The Raman spectrum shows two broad peaks, corresponding to D and G bands, appearing at 1354 and 1580  $\text{cm}^{-1}$  for Na–MaFDHC and 1325 and 1595  $\text{cm}^{-1}$  for Zn–MaFDHC, respectively. The presence of a 2D band around  $\sim 2800 \text{ cm}^{-1}$  also affirms the disordered carbon structure. The  $I_D/I_G$  ratio of the raw MaF was calculated to be 0.77. This also confirms the disordered nature of the raw MaF material. Due to these disordered properties, it can efficiently act as an anode material for sodium-ion batteries. The  $I_D/I_G$  ratio of Na–MaFDHC and Zn–MaFDHC are 0.85 and 0.83, respectively. The  $I_D/I_G$  ratio never goes above one, which designates that the ordered graphene sheets in all the materials are highly disordered, i.e., non-graphitizable. Tuinstra and Koenig analyze the link between in-plane correlation length  $L_a$  and intensity ratio  $\frac{I_D}{I_G}$  for carbonaceous materials [39]. The equation is given by

$$L_a = 2.4 \times 10^{-10} \left( \lambda \times \frac{I_G}{I_D} \right) \quad (1)$$

where  $L_a$  is the in-plane correlation length that gives the structural order arranged in the plane of porous carbon materials.  $\lambda$  represents the coefficient of excited wavelength (532.9 nm) [40]. From the above equation, the calculated values of Na–MaFDHC and Zn–MaFDHC are 150.21 nm and 153.83 nm, respectively, representing the median plane length of the prepared material. Thus, the Raman spectra confirm the existence of hard carbon, which is suitable for the Na intercalation/deintercalation process.

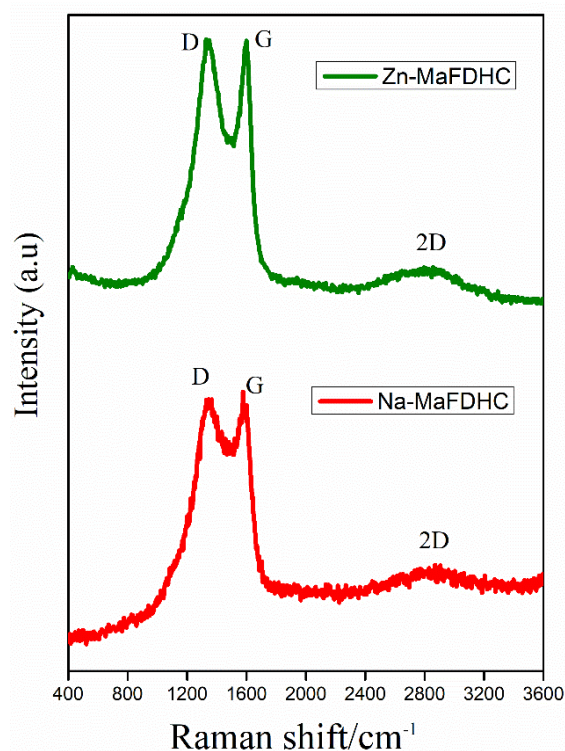


**Figure 3.** RAMAN spectra of Na–MaFDHC and Zn–MaFDHC powders.

Figure 4 shows the typical BET isotherms of both samples and Table 1 gives the value of pore diameter and the surface area of the synthesized HC materials alongside

the earlier reports. Figures S5 and S6 show the BET isotherms of raw MaF. In addition, a nitrogen adsorption plot for Na–MaFDHC and Zn–MaFDHC is shown in Figure S7. This Figure also explains the linear relationship between  $1/[W((P_0/P) - 1)]$  and  $P/P_0$ . Figure 4a explains the correlation between the cumulative differential pore volume (DV) and pore width of the materials [41]. Basically, the DV curve is the true pore volume distribution that is a function of pore diameter. The surface area of the untreated MaFDHC is  $18 \text{ m}^2 \text{ g}^{-1}$ . The results varied when compared to the already reported surface area, and pore diameter of *MaF* without activation and activated with KOH and  $\text{ZnCl}_2$  [42], owing to the increased temperature of the as-prepared samples. Generally, temperature plays a major role in the carbonization process. In our case, the HC, when treated with NaOH and  $\text{ZnCl}_2$ , shows a surface area of 45.02 and  $351 \text{ m}^2 \text{ g}^{-1}$ , respectively. The surface area increase is significant because of the action of porogens (unreactive agents). The surface area also plays a remarkable role in improving the electrochemical performance of the MaFDHC samples. The pore diameter of the carbon materials has shown a significant increase after the treatment of activating agents. Subramanian et al. [42] reported that the untreated *MaFDHC* shows pore diameter of 1.9 nm, but KOH treated and  $\text{ZnCl}_2$  treated samples exhibit pore diameter of 2.5 and 2.3 nm, respectively. In the present case, the raw MaF exhibits the pore diameter of 2.1 nm. Na–MaFDHC and Zn–MaFDHC show the pore diameter of 3.611 and 3.757 nm. Here, the surface area and pore diameter were both influenced by the activating agent due to its dehydrating nature when compared to Na. This further confirms the influence of activating agents in the as-prepared HC materials. The hysteresis observed in  $\text{N}_2$  adsorption/desorption isotherms is primarily a result of the mesoporous nature of the prepared MaFDHC materials. The mechanism behind the chemicals used ( $\text{NaOH}/\text{ZnCl}_2$ ) for activation is well-known for various carbon materials. In carbon materials, the pore generation is chiefly owing to a few active sites in the raw materials that are selectively etched by the strong corrosive nature of NaOH at high temperatures [43]. In the pyrolysis processes, the basic pore structure is formed by eliminating non-carbon atoms. This hampers the subsequent activation process with NaOH to create a porous structure. In  $\text{ZnCl}_2$ , during pyrolysis, it performs as a dehydrating agent and yields porous nature in the raw material where carbon's aromatization and charring occur. After pyrolysis, the unreacted  $\text{ZnCl}_2$  can be washed and removed, resulting in further pore generation [44]. In MaFDHC materials, mesoporous structures exist. Compared to NaOH, the activation of hydrochars with  $\text{ZnCl}_2$  effectively enhances the porosity of the synthesized carbonaceous material [45].

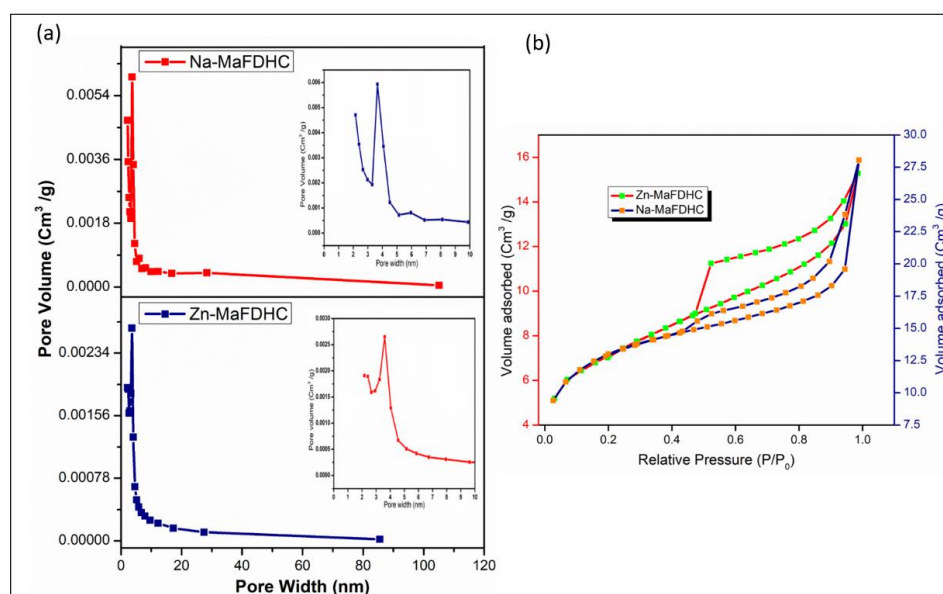


**Figure 4.** (a) Pore size distribution and (b)  $\text{N}_2$  adsorption and desorption isotherms of Na–MaFDHC and Zn–MaFDHC powders.

**Table 1.** Textural properties of MaFDHC samples compared with reported data.

No	Sample	Surface Area (m <sup>2</sup> g <sup>-1</sup> )	Pore Diameter (nm)	Pore Volume (cc g <sup>-1</sup> )
Reference [42]	MaFDHC without activation,	36	1.9	Not Reported
	10% of KOH treated,	386	2.5	
	10% of ZnCl <sub>2</sub> treated.	1097	2.3	
1	Raw MaF	18	2.1	0.009
2	Na—MaFDHC	45.02	3.611	0.029
3	Zn—MaFDHC	351	3.757	0.017

The SEM images of the synthesized sample are shown in Figure 5a,b. Figure S8 shows the SEM image of raw MaF. The surface morphology of the obtained HC materials is a prime factor for electrochemical performance when used as an electrode anode material in NIBs. The activation agents are used here to improve the pore structure of MaFDHC. Before activation, the raw fiber shows the morphology of micrometer sized large fiber stacks. After activation, the disordered and uneven morphologies were observed in the images. The as-prepared Na—MaFDHC shows the irregular and disordered porous structure, while Zn—MaFDHC clearly shows the mesoporous structure. The SEM image of Zn—MaFDHC Figure 5b has shown a more porous structure when compared to Na—MaFDHC, when compared to raw MaF. Figure 5a shows this visibly. It is palpable that bushy walls become opened, and an extensive porosity is fashioned; thus, the chemically activated carbons' peripheral surface areas are full of cavities. Pores with different shapes and different sizes were attained from the activating agents. In this case, the NaOH paves the way for the surface deformation of the raw materials [46]. The BET analysis has been discussed briefly above for further confirmation of pore diameter and pore volume. It should be known that all kinds of pores may not be helpful for battery applications. Mesopores, micropores and macropores are more helpful for ion transfer and electrolyte diffusion; therefore, they reveal performance as NIB anodes.

Figure 5c,d show the TEM images of MaFDHC samples. Figure S9 shows the TEM image of raw MaF. They demonstrate the well-defined larger mesopores throughout the particle structures. The Raw MaF also divulges the amorphous nature of the fibrous material. A defective and disordered structure was observed in the images as predictable for hard carbons. The TEM images further confirm the amorphous and disordered nature of MaFDHC. The expansion of a locally ordered structure comprising nano graphitic domains could be observed by varying the activating agents. The TEM results are well correlated by XRD, Raman spectroscopy, and the pore size distribution from BET measurement by N<sub>2</sub> adsorption. For a typical HC, the material is analyzed through the occurrence of turbostratic graphitic domains dispersed in a non-carbon matrix [47,48].

The sodium can be intercalated into the defects, which are created by the hetero atoms such as N and O. The Na metal can fill in the pores that can be created by the activating agents. The Na adsorption on the disordered graphene sheets ensues in a sloping potential between 1 and 0.1 V [49]. Figure 6a–e demonstrate the cyclic voltammetry (CV), galvanostatic charge/discharge (GCD) and cycling performance of both MaFDHC anodes. Figure S10 shows the electrochemical impedance spectroscopy of raw MaF. This reveals the conductivity of the raw MaF. The first three cycles of the CV curves for the prepared samples are shown in Figure 6a,b. The CV curves show no sharp peaks. The sharp peaks are the accredited forming of a solid electrolyte interface (SEI) layer [47]. The lower surface area of the sample may result in the limited formation of SEI. However, here, when we compare NaOH and ZnCl<sub>2</sub> treated material, the Zn—MaFDHC achieves a higher surface area than Na—MaFDHC. This is due to the action of porogens, i.e., activating agents. The Initial Coulombic Efficiency (ICE) of Na—MaFDHC and Zn—MaFDHC are found as 98.8% and

99.7%. This high ICE is because of fewer oxygenated groups present in the as prepared Zn–MaFDHC material. Along with the BET results, the functional groups of carbon also seem to be affecting capacity. Here, the Zn–MaFDHC cell exhibited a better cycling performance compared to the Na–MaFDHC cell. This demonstrates the durability of the adsorption and desorption of sodium storage in a manner similar to the supercapacitor materials [50,51].

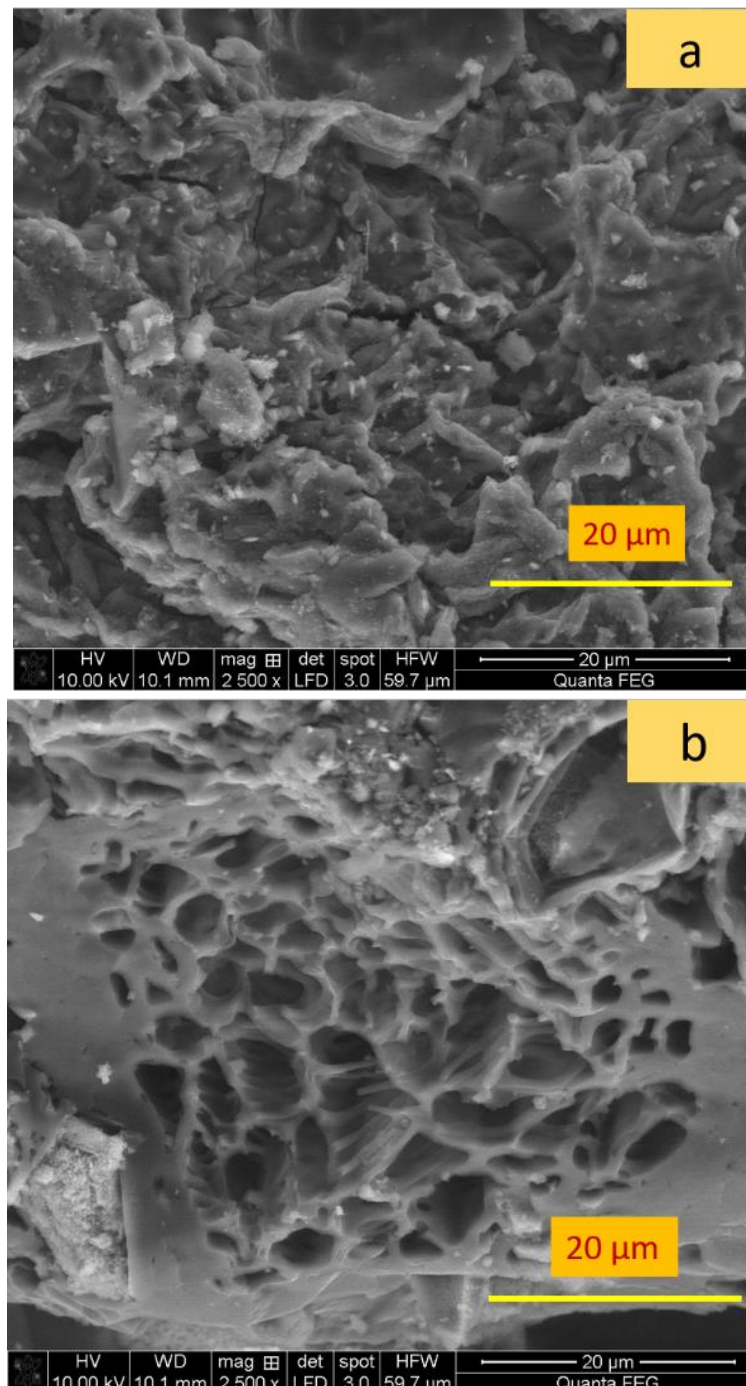
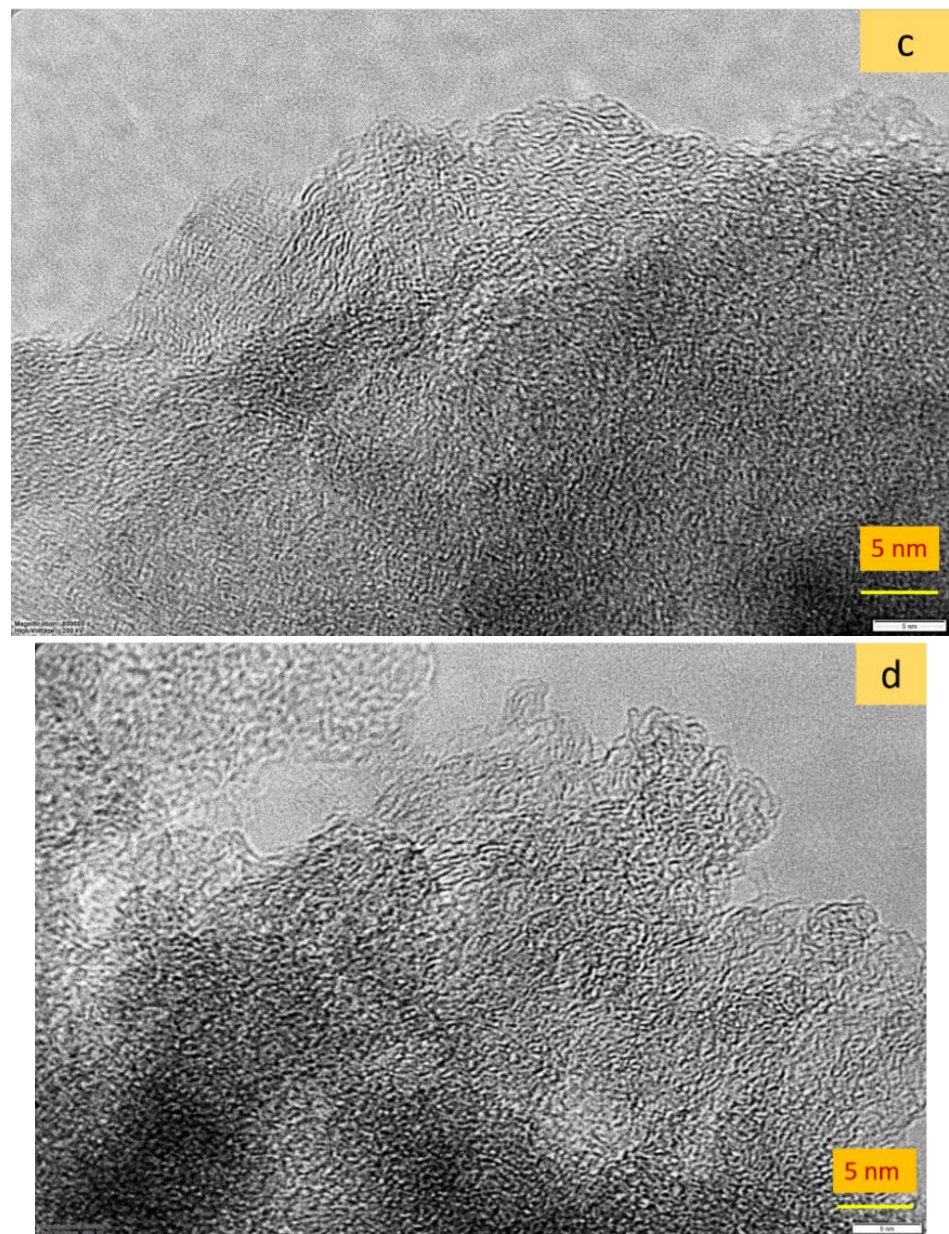


Figure 5. Cont.



**Figure 5.** SEM images of (a) Na–MaFDHC, (b) Zn–MaFDHC. TEM images of (c) Na–MaFDHC, (d) Zn–MaFDHC.

Figure S10 shows the electrochemical impedance spectroscopy (EIS) of the Raw MaF. EIS was used to analyze the conductivity of the raw MaF material. The Figure reveals the  $R_{CT}$  value in Mohm, which has very high impedance. Figure 6f shows the electrochemical impedance spectra of Na–MaFDHC and Zn–MaFDHC cells after 100 cycles. It shows a semicircle accompanied by an inclined line. The intercept of the high-frequency region states the overall amount of ohmic resistance to the cell, mainly electrolyte resistance [52]. The large semicircle affirms the charge transfer resistance of the cell couple for the synthesized material. The inclined plane corresponds to the Warburg impedance, which shows the diffusion process. The diffusion coefficient of Na–MaFDHC and Zn–MaFDHC was calculated by using the formula

$$D_{Na^+} = \frac{R^2 T^2}{2A^2 n^2 F^4 C^2 \sigma^2}$$

where  $R$  is the gas constant,  $T$  is the absolute temperature,  $n$  represents the number of electrons transferred,  $F$  represents the Faraday constant,  $A$  is the area of electrode ( $0.785 \text{ cm}^2$ ), and  $\sigma$  represents the Warburg resistance. The  $R_{CT}$ ,  $R_S$ , and  $D_{Na^+}$  are listed in Table S2. From the Figure S10 and Figure 6f, and Table S2, it is confirmed that the raw MaF material was induced by the activating agent and behaves as an anode material that shows the better electrochemical performance of batteries. Li et al. [53] reported that the synthesized HC electrode obtained the reversible capacity of  $88 \text{ mAh g}^{-1}$  at a  $0.1 \text{ C}$  rate, with a tremendously low CE of 26%. In the present case, at the  $1 \text{ C}$  rate, the Na–MaFDHC and Zn–MaFDHC exhibit a reversible capacity of 103 to 45  $\text{mAh g}^{-1}$  and 114 to 69  $\text{mAh g}^{-1}$ , respectively, for the first and 100th cycles. After 100 cycles, the Zn–MaFDHC shows a better capacity retention of 61% compared to Na–MaFDHC (43%), which corroborates the better electrochemical performance of the material activated with  $\text{ZnCl}_2$ . This could be because the MaF is a lignocellulosic material with a greater oxygen content, and the  $\text{ZnCl}_2$  is an acetic reagent that is capable of interacting with functional groups in MaF, thus catalyzing dehydration reactions, resulting in charring [54]. Based on this mechanism, the material Zn–MaFDHC shows good reversible capacity, initial CE, and capacity retention, which reveals better electrochemical performances as an anode of NIBs. Furthermore, the X-ray diffraction analysis was carried out for the electrode anode materials after 100 cycles. It was observed that even after 100 cycles, the structural stability was stable, as shown in Figure S11.

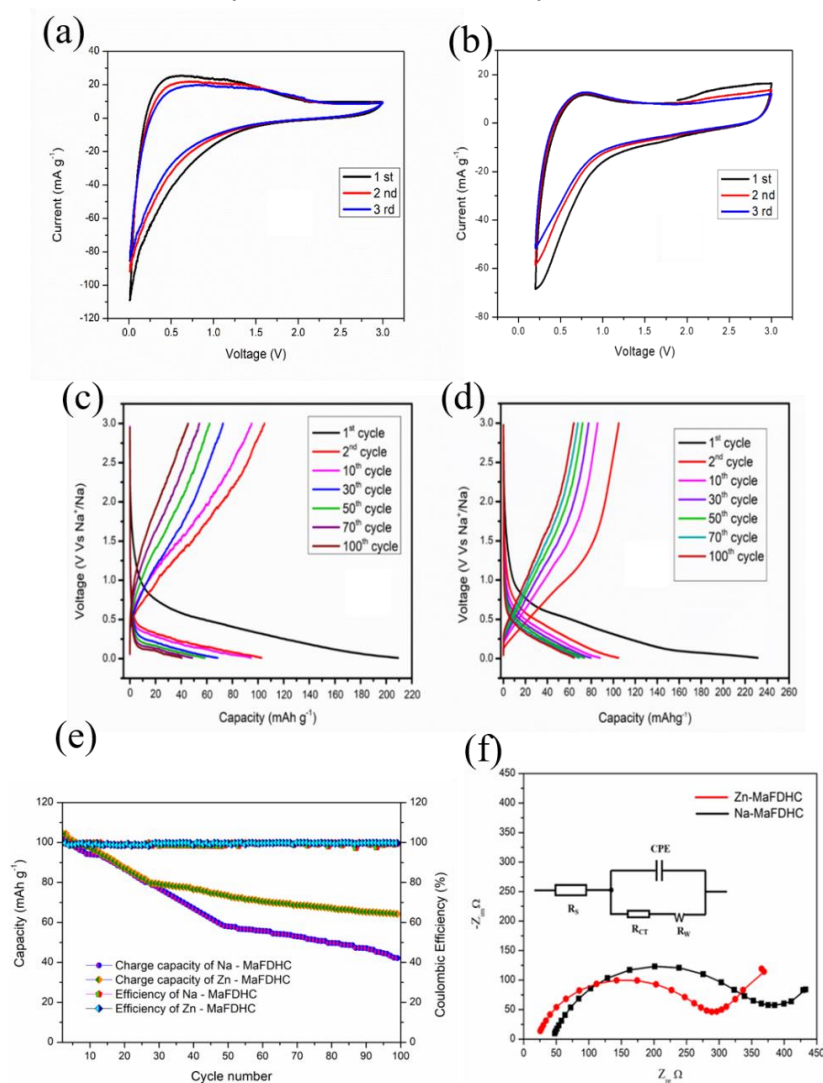


**Figure 6.** Cyclic Voltammetry for (a) Na–MaFDHC and (b) Zn–MaFDHC. Galvanostatic charge/discharge performance of (c) Na–MaFDHC, (d) Zn–MaFDHC. (e) Cyclic performance and efficiency of MaFDHC cells. (f) Nyquist plot of MaFDHC cells.

#### 4. Conclusions

In this study, for the first time, an attempt has been made to obtain the HC derived from *MaF* precursor prepared via the combination of pyrolysis and activation methods and to study their electrochemical performance. Herein, the material *MaFDHC* has a higher interlayer spacing when compared to graphite. The sample was analyzed for its disordered structure by XRD, RAMAN, and its textural properties by the  $N_2$  adsorption and desorption process. The activating agents produced more pores in the HC materials and led to a better ion transfer process. The Zn–*MaFDHC* material retained a higher charge capacity ( $114 \text{ mAh g}^{-1}$ ) than Na–*MaFDHC* ( $103 \text{ mAh g}^{-1}$ ) due to its Zn dehydrating properties in the carbon matrix. Moreover, the synthesized material Zn–*MaFDHC* retains its capacity of 61%, revealing good cyclability after 100 cycles. From this analysis, using  $ZnCl_2$  as an activation agent showed better effects on the material and electrochemical characterizations of HC for NIB applications. We believe much better performance could be achieved with further optimizations with electrode compositions and mass loadings, which could be interesting for future studies.

**Supplementary Materials:** The following supporting information can be downloaded at: <https://www.mdpi.com/article/10.3390/en16020979/s1>, Figure S1: Bar graph for various Fibers and their Width; Figure S2: Bar graph for various fibers and their elongations; Figure S3: XRD pattern of Raw *MaF*; Figure S4: Raman spectra of Raw *MaF*; Figure S5: Nitrogen adsorption and desorption of raw *MaF*; Figure S6: Pore size distribution of raw *MaF*; Figure S7: Nitrogen adsorption plot for Na–*MaFDHC* and Zn–*MaFDHC*; Figure S8: SEM image of raw *MaF*; Figure S9: TEM image of Raw *MaF*; Figure S10: Nyquist plot of Raw *MaF*; Figure S11: XRD images of Na–*MaFDHC* and Zn–*MaFDHC* after 100 cycles. Table S1: Physical property of natural fibers; Table S2: Sodium-ion Diffusion coefficient of *MaFDHC*.

**Author Contributions:** Conceptualization, M.T., S.R. and S.M.; Methodology, M.T., K.M., S.R. and S.M.; Software, M.T., K.M., S.R. and S.M.; Validation, M.T., K.M., S.R. and S.M.; Formal analysis, M.T., K.M., S.R. and S.M.; Investigation, M.T., K.M., S.R. and S.M.; Resources, M.A. S.R. and S.M.; Data curation, M.T., K.M., S.R. and S.M.; Writing—original draft preparation, M.T., K.M., S.R., M.A. and S.M.; Writing—review and editing, M.T., S.R., M.A. and S.M.; visualization, M.T., K.M., S.R. and S.M.; Supervision S.R. and S.M.; Project administration, S.R. and S.M.; Funding acquisition, S.R., M.A. and S.M. All authors have read and agreed to the published version of the manuscript.

**Funding:** All the authors from Alagappa University acknowledge the financial support by DST SERB, New Delhi, India under the Physical Sciences grant sanctioned vide EMR/2016/006302 and the Ministry of Human Resource Development RUSA Phase 2.0 grant sanctioned vide Lt.No.F-24-51/2014 U Policy (TNMulti Gen), Dept. of Education, Govt. of India. We acknowledge the support by the Open Access Publication Funds of Technische Universität Braunschweig.

**Data Availability Statement:** Not Applicable.

**Conflicts of Interest:** The authors declare no conflict of interest.

#### References

1. Xie, Y.; Fan, M.; Shen, T.; Liu, Q.; Chen, Y.  $SnS_2$  nanoplates as stable anodes for sodium-ion and lithium-ion batteries. *Mater. Technol.* **2016**, *31*, 646–652. [CrossRef]
2. Takashi, J.Y.; Jassiel, R.R.; Vilas, G.P. Waste biomass-derived carbon anode for enhanced lithium storage. *ACS Omega.* **2020**, *5*, 19715–19720.
3. Krishnaveni, K.; Subadevi, R.; Raja, M.; Premkumar, T.; Sivakumar, M. Sulfur/PAN/acetylene black composite prepared by a solution processing technique for lithium-sulfur batteries. *J. Appl. Polym. Sci.* **2018**, *135*, 46598.
4. Xu, X.; Wu, P.; Li, Q.; Yang, W.; Zhang, X.; Wang, X.; Meng, J.; Niu, C.; Mai, L. Realizing stable lithium and sodium storage with high areal capacity using novel nanosheet-assembled compact  $CaV_4O_9$  microflowers. *Nano Energy* **2018**, *50*, 606–614. [CrossRef]
5. Franklin, R.E. Crystallite growth in graphitizing and non-graphitizing carbons. Proceedings of the Royal Society of London. *Ser. A Math. Phys. Sci.* **1951**, *209*, 196–218.
6. Luo, Y.; Tang, Y.; Zheng, S.; Yan, Y.; Xue, H.; Pang, H. Dual anode materials for lithium-and sodium-ion batteries. *J. Mater. Chem. A* **2018**, *6*, 4236. [CrossRef]

7. Kouthaman, M.; Arjunan, P.; Kannan, K.; Priyanka, V.; Subadevi, R.; Kumaran, V.; Gnanamuthu, R.M.; Sivakumar, M. Enhancing structural stability of layered O<sub>3</sub>-type Na-Mn-Ni-Cu-O cathode material through copper substitution for sodium batteries. *J. Taiwan Inst. Chem. Eng.* **2020**, *117*, 86–92. [[CrossRef](#)]
8. Lotfabad, E.M.; Ding, J.; Cui, K.; Kohandehghan, A.; Kalisvaart, W.P.; Hazelton, M.; Mitlin, D. High-density sodium and lithium-ion battery anodes from banana peels. *ACS Nano* **2014**, *8*, 7115–7129. [[CrossRef](#)]
9. Ahuja, V.; Senthilkumar, B.; Senguttuvan, P. Ultra-stable Sb/hard carbon composite anodes with synergistic alkali-ion storage performances. *Mater. Res. Bull.* **2021**, *144*, 111491. [[CrossRef](#)]
10. Kannan, K.; Kouthaman, M.; Arjunan, P.; Subadevi, R.; Sivakumar, M. Titanium based layered O<sub>3</sub>-NaTi<sub>7/10</sub>Ni<sub>3/20</sub>Mg<sub>3/20</sub>O<sub>2</sub> anode material for sodium ion batteries. *Mater. Lett.* **2020**, *273*, 127950. [[CrossRef](#)]
11. Arjunan, P.; Kouthaman, M.; Kannan, K.; Diwakar, K.; Priyanka, V.; Subadevi, R.; Sivakumar, M. Study on Efficient Electrode from Electronic waste renewed carbon material for sodium battery applications. *J. Environ. Chem. Eng.* **2021**, *9*, 105024. [[CrossRef](#)]
12. Wu, F.C.; Tseng, R.L.; Juang, R.S. Preparation of highly microporous carbons from fir wood by KOH activation for adsorption of dyes and phenols from water. *Sep. Purif. Technol.* **2005**, *47*, 10–19. [[CrossRef](#)]
13. Mahmoudi, K.; Hamdi, N. Preparation and characterization of activated carbon from date pits by chemical activation with zinc chloride for methyl orange adsorption. *J. Mater. Environ. Sci.* **2014**, *51*, 758–1769.
14. Pelaez-Cid, A.A.; Teutli-Leon, M.M.M. *Lignocellulosic Precursors Used in the Synthesis of Activated Carbon: Characterization Techniques and Applications in the Wastewater Treatment*, 1st ed.; Montoya, V.H., Bonilla-Petriciolet, A., Eds.; InTech: Rijeka, Croatia, 2012.
15. Pereira, R.G.; Veloso, C.M.; Da Silva, N.M.; De Sousa, L.F.; Bonomo, R.C.F.; De Souza, A.O.; Souza, M.O.D.G.; Fontan, R.D.C.I. Preparation of activated carbons from cocoa shells and siriguela seeds using H<sub>3</sub>PO<sub>4</sub> and ZnCl<sub>2</sub> as activating agents for BSA and lactalbumin adsorption. *Fuel Process. Technol.* **2014**, *126*, 476–486. [[CrossRef](#)]
16. Teo, E.Y.L.; Muniandy, L.; Ng, E.P.; Adam, F.; Mohamed, A.R.; Jose, R.; Chong, K.F. High surface area activated carbon from rice husk as a high-performance supercapacitor electrode. *Electrochem. Acta* **2016**, *192*, 110–119. [[CrossRef](#)]
17. Abdel-Ghani, N.T.; El-Chaghaby, G.A.; El Gamma, M.H.; Rawash, E.A. Optimizing the preparation conditions of activated carbons from olive cake using KOH activation. *New Carbon Mater.* **2016**, *31*, 2–10. [[CrossRef](#)]
18. Yahya, M.A.; Al-Qodah, Z.; Ngah, C.W.Z. Agricultural bio-waste materials as potential sustainable precursors used for activated carbon production: A review. *Renew. Sustain. Energy Rev.* **2015**, *46*, 218–235. [[CrossRef](#)]
19. Rafatullah, M.; Ahmad, T.; Ghazali, A.; Sulaiman, O.; Danish, M.; Hashim, R. Oil palm biomass as a precursor of activated carbons: A review. *Crit. Rev. Environ. Sci. Technol.* **2013**, *43*, 1117–1161. [[CrossRef](#)]
20. Wirasnita, R.; Hadibarata, T.; Yusoff, A.R.M.; Mat, L.Z. Preparation and characterization of activated carbon from oil palm empty fruit bunch wastes using zinc chloride. *J. Teknol.* **2015**, *74*, 77–81. [[CrossRef](#)]
21. Demiral, H.; Demiral, I.; Karabacako, G.B.; Tumsek, F. Production of activated carbon from olive bagasse by physical activation. *Chem. Eng. Res. Des.* **2011**, *89*, 206–213. [[CrossRef](#)]
22. Hussein, M.Z.; Abdul Rahman, M.B.; Yahaya, A.H.; Taufiq-Yap, Y.H.; Ahmad, N. Oil palm trunk as a raw material for activated carbon production. *J. Porous Mater.* **2001**, *8*, 327–334. [[CrossRef](#)]
23. Meenatchi, T.; Priyanka, V.; Subadevi, R.; Liu, W.R.; Huang, C.H.; Sivakumar, M. Probe on hard carbon electrode derived from orange peel for energy storage application. *Carbon Lett.* **2021**, *31*, 1033–1039. [[CrossRef](#)]
24. Ranaweera, C.K.; Kahol, P.K.; Ghimire, M.; Mishra, S.R.; Gupta, R.K. Orange-peel-derived carbon: Designing sustainable and high-performance supercapacitor electrodes. *J. Carbon Res.* **2017**, *3*, 25. [[CrossRef](#)]
25. Zhu, Y.; Xiang, X.; Liu, E.; Wu, Y.; Xie, H.; Wu, Z.; Tian, Y. An activated microporous carbon prepared from phenol-melamine-formaldehyde resin for lithium-ion battery anode. *Mater. Res. Bull.* **2012**, *47*, 2045–2050. [[CrossRef](#)]
26. Thenappan, M.; Rengapillai, S.; Marimuthu, S. Hard carbon repressing porous morphology derived from coconut sheath for sodium-ion battery. *Energies* **2022**, *15*, 8086. [[CrossRef](#)]
27. Subagyo, A.; Chafidz, A. Banana pseudo-stem fiber: Preparation, characteristics, and applications. *Banan. Nutr.-Funct. Process. Kinet.* **2018**, *10*, 1–19.
28. Ahmad, T.; Danish, M. Prospects of banana waste utilization in wastewater treatment: A review. *J. Environ. Manag.* **2018**, *206*, 330–348. [[CrossRef](#)]
29. Venkateshwaran, N.; Ayyasamy, E. Banana fiber reinforced polymer composites—A Review. *J. Reinf. Plast. Compos.* **2010**, *29*, 2387–2396. [[CrossRef](#)]
30. Srinivasan, V.S.; Boopathy, S.R.; Sangeetha, D.; Ramnath, B.V. Evaluation of mechanical and thermal properties of banana-flax-based natural fiber composite. *Mater. Des.* **2014**, *60*, 620–627. [[CrossRef](#)]
31. Subramanya, R.; Satyanarayana, K.G.; Shetty Pilar, B. Evaluation of structural tensile and thermal properties of banana fibers. *J. Natural Fibers* **2017**, *14*, 485–497.
32. Oliveira, G.F.D.; Andrade, R.C.D.; Trindade, M.A.G.; Andrade, H.M.C.; Carvalho, C.T.D. Thermogravimetric and spectroscopic study (TG-DTA/FT-IR) of activated carbon from the renewable biomass source babassu. *Quimica Nova* **2017**, *40*, 284–292. [[CrossRef](#)]
33. Parre, A.; Karthikeyan, B.; Balaji, A.; Udhayasankar, R. Investigation of chemical, thermal and morphological properties of untreated and NaOH treated banana fiber. *Mater. Today Proc.* **2020**, *22*, 347–352. [[CrossRef](#)]
34. Periera, P.H.F.; Benini, K.C.C.C.; Watashi, C.Y.; Voorwald, H.J.C.; Cioffi, M.O.H. Characterization of high density Polyethylene (HDPE) Reinforced with Banana peel fibers. *Bioresources* **2013**, *8*, 2351–2365. [[CrossRef](#)]

35. Wang, Z.; Qie, L.; Yuan, L.; Zhang, W.; Hu, X.; Huang, Y. Functionalized N-doped interconnected carbon nanofibers as an anode material for sodium-ion storage with excellent performance. *Carbon* **2013**, *55*, 328–334. [[CrossRef](#)]
36. Taer, E.; Taslim, R.; Aini, Z.; Hartati, S.D.; Mustika, W.S. Activated carbon electrode from banana-peel waste for supercapacitor applications. In Proceedings of the 6th International conference on theoretical and applied physics, Yogyakarta, Indonesia, 6–8 September 2017; p. 040004-1-5.
37. Priyanka, V.; Savithiri, G.; Subadevi, R.; Suryanarayanan, V.; Sivakumar, M. Physicochemical Exfoliation of Graphene Sheets using Graphitic Carbon Nitride. *New J. Chem.* **2019**, *43*, 16200–16206. [[CrossRef](#)]
38. Wang, Y.X.; Chou, S.L.; Liu, H.K.; Dou, S.X. Reduced graphene oxide with superior cycling stability and rate capability for sodium storage. *Carbon* **2013**, *57*, 202–208. [[CrossRef](#)]
39. Panitz, J.C.; Novak, P. Raman microscopy of a quality control tool for electrodes for lithium-ion batteries. *J. Power Sources* **2000**, *97*, 174–180. [[CrossRef](#)]
40. Diwakar, K.; Rajkumar, P.; Arjunan, P.; Liu, W.R.; Huang, C.H.; Subadevi, R.; Sivakumar, M. Eggshell—Membrane—Derived carbon coated on Li<sub>2</sub>FeSiO<sub>4</sub> cathode materials for Li-ion batteries. *Appl. Energy Mater.* **2020**, *13*, 786.
41. Liu, K.; Ostadhassan, M. The impact of pore size distribution data presentation format on pore structure interpretation on shales. *Adv. Geo-Energy Res.* **2019**, *3*, 187–197. [[CrossRef](#)]
42. Subramanian, V.; Luo, C.; Stephan, A.M.; Nahm, K.S.; Thomas, S.; Wei, B. Supercapacitors from activated carbon derived from banana fibers. *J. Phys. Chem. C* **2007**, *111*, 7527–7531. [[CrossRef](#)]
43. Lillo-Rodenas, M.A.; Juan-Juan, J.; Cazorla-Amoros, D.; Linares-Solano, A. About reactions occurring during chemical activation with hydroxides. *Carbon* **2004**, *42*, 1371–1375. [[CrossRef](#)]
44. Xu, B.; Chen, Y.; Wei, G.; Cao, G.; Zhang, H.; Yang, Y. Activated carbon with high capacitance prepared by NaOH activation for supercapacitors. *Mater. Chem. Phys.* **2010**, *124*, 504–509. [[CrossRef](#)]
45. Harmas, M. Effect of Zinc chloride activation on D-Glucose derived carbons-based capacitors performance in ionic liquid. *J. Electrochem. Soc.* **2020**, *167*, 080533. [[CrossRef](#)]
46. Kulic, M.; Varol, E.A.; Putun, A.E. Preparation and surface characterization of activated carbons from euphorbia rigida by chemical activation with ZnCl<sub>2</sub>, K<sub>2</sub>CO<sub>3</sub>, NaOH and H<sub>3</sub>PO<sub>4</sub>. *Appl. Surf. Sci.* **2012**, *261*, 247–254. [[CrossRef](#)]
47. Zhang, T.; Mao, J.; Liu, X.; Xuan, M.; Bi, K.; Zhang, X.L.; Hu, J.; Fan, J.; Chen, S.; Shao, G. Pinecone biomass-derived Hard carbon anodes for high-performance sodium-ion batteries. *RSC Adv.* **2017**, *7*, 41504–41511. [[CrossRef](#)]
48. Xiao, L.; Lu, H.; Fang, Y.; Sushko, M.L.; Cao, Y.; Ai, X.; Yang, H.; Liu, J. Low-defect and low-porosity hard carbon with high coulombic efficiency and high capacity for practical sodium ion battery anode. *Adv. Energy Mater.* **2018**, *8*, 1703238. [[CrossRef](#)]
49. Gorka, J.; Vix-Guterl, C.; Ghimbeu, C.M. Recent progress in design of biomass-derived hardcarbons for sodium-ion batteries. *J. Carbon Res.* **2016**, *2*, 1–17.
50. Mozzaffar, A.; Huang, S.S.; Lin, Y.H.; Lin, Y.C.; Shih, B.Y.; Sheu, H.S.; Liao, Y.F.; Wu, N.L. High performance carbon—Coated ZnMn<sub>2</sub>O<sub>4</sub> nNocrystallite supercapacitors with tailored microstructures enabled by novel solution combustion method. *J. Power Sources* **2018**, *378*, 90–97.
51. Mozzaffar, A.; Liu, H.W.; Lin, C.H.; Weng, Y.T.; Sheu, H.S.; Lee, J.F.; Lu, M.L.; Liao, Y.F.; Wu, N.L. Enabling extraordinary rate performance for poorly conductive oxide pseudocapacitors. *Energy Environ. Mater.* **2020**, *3*, 405–413.
52. Xie, J.; Yang, P.; Wang, Y.; Qi, T.; Lei, Y.; Li, C.M. Puzzles and confusions in supercapacitor and battery: Theory and solutions. *J. Power Sources* **2018**, *40*, 213–223. [[CrossRef](#)]
53. Li, Y.; Hu, Y.S.; Titirici, M.M.; Chen, L.; Huang, X. Hard carbon microtubes made from renewable cotton as high-performance anode material for sodium-ion batteries. *Adv. Energy Mater.* **2016**, *6*, 1600659. [[CrossRef](#)]
54. Suhdi Wang, S.C. Fine activated carbon from rubber fruit shell prepared by using ZnCl<sub>2</sub> and KOH activation. *Appl. Sci.* **2021**, *11*, 3994. [[CrossRef](#)]

**Disclaimer/Publisher’s Note:** The statements, opinions and data contained in all publications are solely those of the individual author(s) and contributor(s) and not of MDPI and/or the editor(s). MDPI and/or the editor(s) disclaim responsibility for any injury to people or property resulting from any ideas, methods, instructions or products referred to in the content.